



Efficient wireless *non-radiative mid-range* energy transfer

Aristeidis Karalis^{a,*}, J.D. Joannopoulos^b, Marin Soljačić^b

^a *Department of Electrical Engineering and Computer Science, Massachusetts Institute of Technology, 77 Massachusetts Avenue, Cambridge, MA 02139, USA*

^b *Department of Physics, Massachusetts Institute of Technology, 77 Massachusetts Avenue, Cambridge, MA 02139, USA*

Received 17 April 2007; accepted 17 April 2007
Available online 27 April 2007

Abstract

We investigate whether, and to what extent, the physical phenomenon of long-lifetime resonant electromagnetic states with localized slowly-evanescent field patterns can be used to transfer energy efficiently over non-negligible distances, even in the presence of extraneous environmental objects. Via detailed theoretical and numerical analyses of typical real-world model-situations and realistic material parameters, we establish that such a non-radiative scheme can lead to “strong coupling” between two medium-range distant such states and thus could indeed be practical for efficient medium-range wireless energy transfer.

© 2007 Elsevier Inc. All rights reserved.

Keywords: Wireless energy; Wireless power; Strong coupling

1. Introduction

In the early days of electromagnetism, before the electrical-wire grid was deployed, serious interest and effort was devoted (most notably by Nikola Tesla [1]) towards the development of schemes to transport energy over long distances without any carrier medium (e.g. wirelessly). These efforts appear to have met with little success. Radiative modes of

* Corresponding author. Fax: +1 617 253 2562.
E-mail address: aristos@mit.edu (A. Karalis).

omni-directional antennas (which work very well for information transfer) are not suitable for such energy transfer, because a vast majority of energy is wasted into free space. Directed radiation modes, using lasers or highly-directional antennas, can be efficiently used for energy transfer, even for long distances (transfer distance $L_{\text{TRANS}} \gg L_{\text{DEV}}$, where L_{DEV} is the characteristic size of the device), but require existence of an uninterrupted line-of-sight and a complicated tracking system in the case of mobile objects. Rapid development of autonomous electronics of recent years (e.g. laptops, cell-phones, house-hold robots, that all typically rely on chemical energy storage) justifies revisiting investigation of this issue. Today, we face a different challenge than Tesla: since the existing electrical-wire grid carries energy *almost* everywhere, even a medium-range ($L_{\text{TRANS}} \approx \text{few} * L_{\text{DEV}}$) wireless energy transfer would be quite useful for many applications. There are several currently used schemes, which rely on non-radiative modes (magnetic induction), but they are restricted to very close-range ($L_{\text{TRANS}} \ll L_{\text{DEV}}$) or very low-power ($\sim \text{mW}$) energy transfers [2–6].

In contrast to all the above schemes, we investigate the feasibility of using long-lived oscillatory resonant electromagnetic modes, with localized slowly-evanescent field patterns, for efficient wireless *non-radiative mid-range* energy transfer. The proposed method is based on the well known principle of resonant coupling (the fact that two same-frequency resonant objects tend to couple, while interacting weakly with other off-resonant environmental objects) and, in particular, resonant evanescent coupling (where the coupling mechanism is mediated through the overlap of the non-radiative near-fields of the two objects). This well known physics leads trivially to the result that energy can be efficiently coupled between objects in the extremely near field (e.g. in optical waveguide or cavity couplers and in resonant inductive electric transformers). However, it is far from obvious how this same physics performs at mid-range distances and, to our knowledge, there is no work in the literature that demonstrates efficient energy transfer for distances a few times larger than the largest dimension of both objects involved in the transfer. In the present paper, our detailed theoretical and numerical analysis shows that such an efficient mid-range wireless energy-exchange can actually be achieved, while suffering only modest transfer and dissipation of energy into other off-resonant objects, provided the exchange system is carefully designed to operate in a regime of “strong coupling” compared to all intrinsic loss rates. The physics of “strong coupling” is also known but in very different areas, such as those of light-matter interactions [7]. In this favorable operating regime, we quantitatively address the following questions: up to which distances can such a scheme be efficient and how sensitive is it to external perturbations? The omnidirectional but stationary (non-lossy) nature of the near field makes this mechanism suitable for mobile wireless receivers. It could therefore have a variety of possible applications including for example, placing a source (connected to the wired electricity network) on the ceiling of a factory room, while devices (robots, vehicles, computers, or similar) are roaming freely within the room. Other possible applications include electric-engine buses, RFIDs, and perhaps even nano-robots.

2. Range and rate of coupling

The range and rate of the proposed wireless energy-transfer scheme are the first subjects of examination, without considering yet energy drainage from the system for use into work. An appropriate analytical framework for modeling this resonant energy-exchange is that of the well-known coupled-mode theory (CMT) [8]. In this picture, the field of

the system of two resonant objects 1 and 2 is approximated by $\mathbf{F}(\mathbf{r}, t) \approx a_1(t)\mathbf{F}_1(\mathbf{r}) + a_2(t)\mathbf{F}_2(\mathbf{r})$, where $\mathbf{F}_{1,2}(\mathbf{r})$ are the eigenmodes of 1 and 2 alone, and then the field amplitudes $a_1(t)$ and $a_2(t)$ can be shown [8] to satisfy, to lowest order:

$$\begin{aligned} \frac{da_1}{dt} &= -i(\omega_1 - i\Gamma_1)a_1 + i\kappa a_2 \\ \frac{da_2}{dt} &= -i(\omega_2 - i\Gamma_2)a_2 + i\kappa a_1 \end{aligned} \quad (1)$$

where $\omega_{1,2}$ are the individual eigenfrequencies, $\Gamma_{1,2}$ are the resonance widths due to the objects' intrinsic (absorption, radiation, etc.) losses, and κ is the coupling coefficient. Eqs. (1) show that at exact resonance ($\omega_1 = \omega_2$ and $\Gamma_1 = \Gamma_2$), the normal modes of the combined system are split by 2κ ; the energy exchange between the two objects takes place in time $\sim \pi/2\kappa$ and is nearly perfect, apart for losses, which are minimal when the coupling rate is much faster than all loss rates ($\kappa \gg \Gamma_{1,2}$).¹ It is exactly this ratio $\kappa/\sqrt{\Gamma_1\Gamma_2}$ that we will set as our figure-of-merit for any system under consideration for wireless energy-transfer, along with the distance over which this ratio can be achieved. The desired optimal regime $\kappa/\sqrt{\Gamma_1\Gamma_2} \gg 1$ is called “strong-coupling” regime.

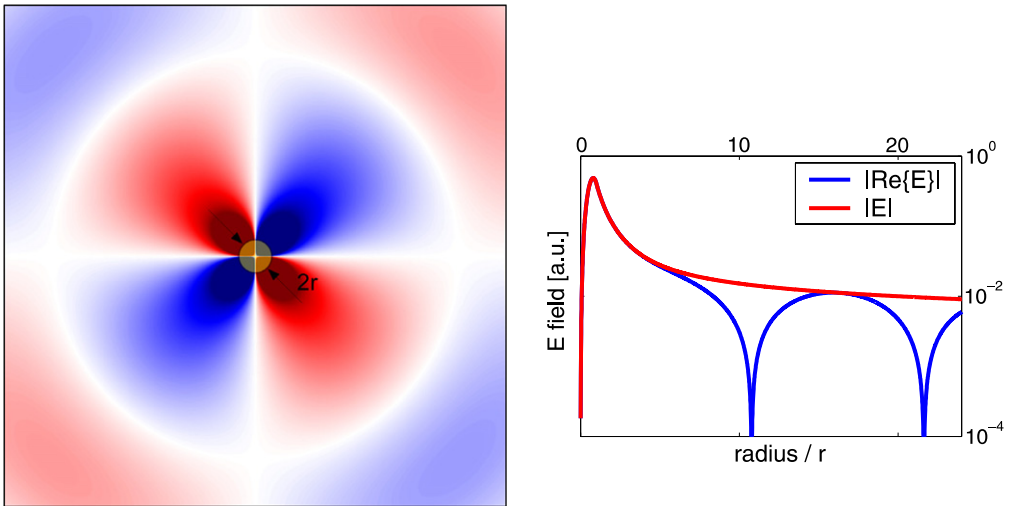
Consequently, our energy-transfer application requires resonant modes of high $Q = \omega/2\Gamma$ for low (slow) intrinsic-loss rates Γ , and this is why we propose a scheme where the coupling is implemented using, not the lossy radiative far-field, but the evanescent (non-lossy) stationary near-field. Furthermore, strong (fast) coupling rate κ is required over distances larger than the characteristic sizes of the objects, and therefore, since the extent of the near-field into the air surrounding a finite-sized resonant object is set typically by the wavelength (and quantified rigorously by the “radiation caustic”), this mid-range non-radiative coupling can only be achieved using resonant objects of subwavelength size, and thus significantly longer evanescent field-tails. This is a regime of operation that has *not* been studied extensively, since one usually prefers short tails to minimize interference with nearby devices. As will be seen in examples later on, such subwavelength resonances can often be accompanied with a high radiation- Q , so this will typically be the appropriate choice for the possibly-mobile resonant device-object d . Note, though, that the resonant source-object s will in practice often be immobile and with less stringent restrictions on its allowed geometry and size, which can be therefore chosen large enough that the near-field extent is not limited by the wavelength (using for example waveguides with guided modes tuned close to the “light line” in air for slow exponential decay therein).

The proposed scheme is very general and *any* type of resonant structure (e.g. electromagnetic, acoustic, nuclear) satisfying the above requirements can be used for its implementation. As examples and for definiteness, we choose to work with two well-known, but quite different, electromagnetic resonant systems: dielectric disks and capacitively-loaded conducting-wire loops. Even without optimization, and despite their simplicity, both will be shown to exhibit acceptably good performance.

¹ The CMT model is valid exactly for this optimal operational regime of well-defined resonances. Its range of applicability does not include very-close-distance coupling, since there the necessary condition $\kappa \ll \omega_{1,2}$ does not hold, neither large-distance far-field coupling, since it fails to predict far-field interference effects and accurate radiation patterns; rather CMT is exactly suitable for the medium-distance near-field coupling of our interest. Thus the use of this model is justified and the parameters κ , $\Gamma_{1,2}$ are well defined.

2.1. Dielectric disks

Consider a 2D dielectric disk object of radius r and relative permittivity ϵ surrounded by air that supports high- Q “whispering-gallery” resonant modes (Fig. 1). The loss mechanisms for the energy stored inside such a resonant system are radiation into free space and absorption inside the disk material. High- Q^{rad} and long-tailed subwavelength resonances can be achieved, only when the dielectric permittivity ϵ is large and the azimuthal field variations are slow (namely of small principal number m). Material absorption is related to the material loss tangent: $Q^{\text{abs}} \sim \text{Re}\{\epsilon\}/\text{Im}\{\epsilon\}$. Mode-solving calculations for this type of disk resonances were performed using two independent methods: numerically, 2D finite-difference frequency-domain (FDFD) simulations (which solve Maxwell’s Equations in frequency domain exactly apart for spatial discretization) were conducted with a



single disk	λ/r	Q^{abs}	Q^{rad}	Q
Re{ϵ}=147.7, m=2	20.01 (20.00)	10103 (10075)	1988 (1992)	1661 (1663)
Re{ ϵ }=65.6, m=3	9.952 (9.950)	10098 (10087)	9078 (9168)	4780 (4802)

Fig. 1. *Main plot.* A 2D high- ϵ disk of radius r (shown in yellow) surrounded by air, along with the electric field (with polarization pointing out of the page) of its resonant whispering-gallery mode superimposed (shown in red/white/blue in regions of positive/zero/negative field respectively). *Side plot.* Radial plot of the electric field of the mode shown in the main plot (basically a cross-section of the main plot). Note that in air (radius/ $r > 1$) the field follows a Hankel-function form, with an initial exponential-like regime (with long tails compared to the small disk size), followed by the oscillatory/radiation regime (whose presence means that energy is slowly leaking out of the disk). *Table.* Numerical FDFD (and in parentheses analytical SV) results for the wavelength and absorption, radiation and total loss rates, for two different cases of subwavelength-disk resonant modes. Note that disk-material loss-tangent $\text{Im}\{\epsilon\}/\text{Re}\{\epsilon\}=10^{-4}$ was used. (The specific parameters of the plot are highlighted with bold in the table.) Finally, note that for the 3D case the computational complexity would be immensely increased, while the physics would not be significantly different. For example, a spherical object of $\epsilon = 147.7$ has a whispering gallery mode with $m = 2$, $Q^{\text{rad}} = 13,962$, and $\lambda/r = 17$. (For interpretation of the references to color in this figure legend, the reader is referred to the web version of this paper.)

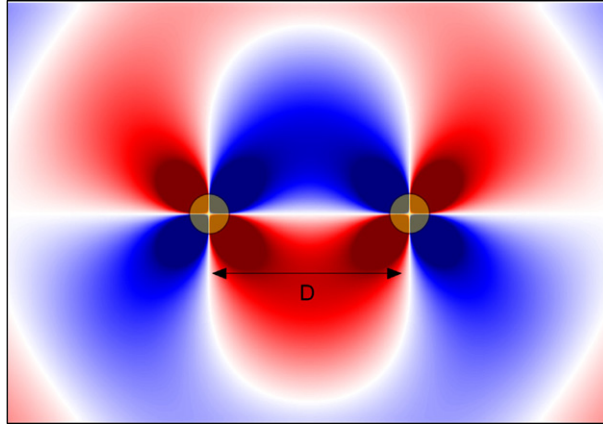
resolution of 30 pts/ r ; analytically, standard separation of variables (SV) in polar coordinates was used. The results for two TE-polarized dielectric-disk subwavelength modes of $\lambda/r \geq 10$ are presented in Fig. 1. The two methods have excellent agreement and imply that for a properly designed resonant low-loss-dielectric object values of $Q^{\text{rad}} \geq 2000$ and $Q^{\text{abs}} \sim 10,000$ should be achievable.

Note that the required values of ε , shown in Fig. 1, might at first seem unrealistically large. However, not only are there in the microwave regime (appropriate for meter-range coupling applications) many materials that have both reasonably high enough dielectric constants and low losses (e.g. Titania: $\varepsilon \approx 96$, $\text{Im}\{\varepsilon\}/\varepsilon \approx 10^{-3}$; Barium tetratitanate: $\varepsilon \approx 37$, $\text{Im}\{\varepsilon\}/\varepsilon \approx 10^{-4}$; Lithium tantalite: $\varepsilon \approx 40$, $\text{Im}\{\varepsilon\}/\varepsilon \approx 10^{-4}$; etc.) [9,10], but also ε could signify instead the effective index of other known subwavelength ($\lambda/r \gg 1$) surface-wave systems, such as surface-plasmon modes on surfaces of metal-like (negative- ε) materials [11] or metallo-dielectric photonic crystals [12].

To calculate now the achievable rate of energy transfer between two disks 1 and 2, we place them at distance D between their centers (Fig. 2). Numerically, the FDFD mode-solver simulations give κ through the frequency splitting ($=2\kappa$) of the normal modes of the combined system, which are even and odd superpositions of the initial single-disk modes; analytically, using the expressions for the separation-of-variables eigenfields $\mathbf{E}_{1,2}(\mathbf{r})$ CMT gives κ through $\kappa = \omega_1/2 \cdot \int d^3\mathbf{r} \varepsilon_2(\mathbf{r}) \mathbf{E}_2^*(\mathbf{r}) \mathbf{E}_1(\mathbf{r}) / \int d^3\mathbf{r} \varepsilon(\mathbf{r}) |\mathbf{E}_1(\mathbf{r})|^2$, where $\varepsilon_j(\mathbf{r})$ and $\varepsilon(\mathbf{r})$ are the dielectric functions that describe only the disk j (minus the constant ε_0 background) and the whole space respectively. Then, for medium distances $D/r = 10\text{--}3$ and for non-radiative coupling such that $D < 2r_C$, where $r_C = m\lambda/2\pi$ is the radius of the radiation caustic, the two methods agree very well, and we finally find (Fig. 2) coupling-to-loss ratios in the range $\kappa/\Gamma \sim 1\text{--}50$. Although the achieved figure-of-merit values do not fall in the ideal “strong-coupling” operating regime $\kappa/\Gamma \gg 1$, they are still large enough to be useful for applications, as we will see later on.

2.2. Capacitively-loaded conducting-wire loops

Consider a loop of radius r of conducting wire with circular cross-section of radius a connected to a pair of conducting parallel plates of area A spaced by distance d via a dielectric of relative permittivity ε and everything surrounded by air (Fig. 3). The wire has inductance L , the plates have capacitance C and then the system has a resonant mode, where the nature of the resonance lies in the periodic exchange of energy from the electric field inside the capacitor, due to the voltage across it, to the magnetic field in free space, due to the current in the wire. Losses in this resonant system consist of ohmic loss R_{abs} inside the wire and radiative loss R_{rad} into free space. Mode-solving calculations for this type of RLC -circuit resonances were performed using again two independent methods: numerically, 3D finite-element frequency-domain (FEFD) simulations (which solve Maxwell’s Equations in frequency domain exactly apart for spatial discretization) were conducted [13], in which the boundaries of the conductor were modeled using a complex impedance $\eta_c = \sqrt{\mu_c \omega / 2\sigma}$ boundary condition, valid as long as $\eta_c/\eta_0 \ll 1$ [14] ($< 10^{-5}$ for copper in the microwave), where μ_0 , ε_0 and $\eta_0 = \sqrt{\mu_0/\varepsilon_0}$ are the magnetic permeability, electric permittivity and impedance of free space and σ is the conductivity of the conductor; analytically, the formulas $L = \mu_0 r [\ln(8r/a) - 2]$ [15] and $C = \varepsilon_0 \varepsilon A/d$, and, in the desired subwavelength-loop ($r \ll \lambda$) limit, the quasi-static formulas $R_{\text{abs}} \approx \eta_c r/a$ (which takes skin-depth effects into account) and $R_{\text{rad}} \approx \pi/6 \eta_0 (r/\lambda)^4$ [15] were used to determine

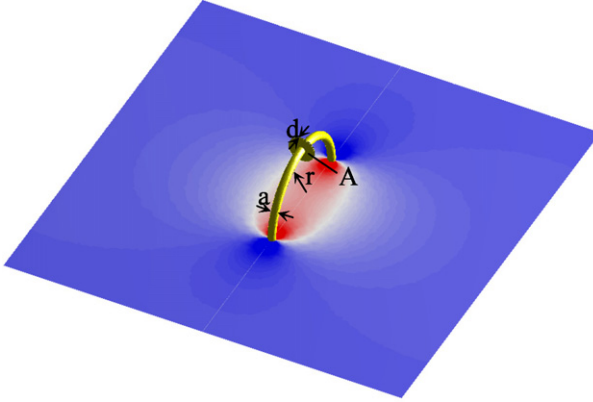


two disks	D/r	Q^{rad}	$Q = \omega/2\Gamma$	$\omega/2\kappa$	κ/Γ
$\text{Re}\{\epsilon\}=147.7, m=2$	3	2478	1989	46.9 (47.5)	42.4 (35.0)
$\lambda/r \approx 20$	5	2411	1946	298.0 (298.0)	6.5 (5.6)
$Q^{abs} \approx 10093$	7	2196	1804	769.7 (770.2)	2.3 (2.2)
	10	2017	1681	1714 (1601)	0.98 (1.04)
$\text{Re}\{\epsilon\}=65.6, m=3$	3	7972	4455	144 (140)	30.9 (34.3)
$\lambda/r \approx 10$	5	9240	4824	2242 (2083)	2.2 (2.3)
$Q^{abs} \approx 10096$	7	9187	4810	7485 (7417)	0.64 (0.65)

Fig. 2. Plot. System of two same 2D high- ϵ disks of radius r (yellow) for medium-distance D coupling between them, along with the electric field of the normal mode, which is an even superposition of the single-disk modes of Fig. 1, superimposed (red/white/blue). Note that there is also a normal mode, which is an odd superposition of the single-disk modes of Fig. 1 (not shown). Table. Numerical FDFD (and in parentheses analytical CMT) results for the average of the wavelength and loss rates of the two normal modes (individual values not shown), and also the coupling rate and “strong/weak-coupling” figure-of-merit as a function of the coupling distance D , for the two cases of disk modes presented in Fig. 1. Only distances for non-radiative ($D < 2r_C$) coupling are considered. Note that the average Γ^{rad} (and thus total Γ) shown are slightly different from the single-disk value of Fig. 1, due to far-field interference effects present for the two normal modes, for which CMT cannot make predictions and this is why analytical results for Γ^{rad} are not shown but the single-disk value is used. (The specific parameters of the plot are highlighted with bold in the table.) (For interpretation of the references to color in this figure legend, the reader is referred to the web version of this paper.)

the resonant frequency $\omega = 1/\sqrt{LC}$ and its quality factors $Q^{abs} = \omega L/R_{abs}$ and $Q^{rad} = \omega L/R_{rad}$. By tuning the capacitance and thus the resonant frequency, the total Q becomes highest for some optimal frequency determined by the loop parameters: at low frequencies it is dominated by ohmic loss and at high frequencies by radiation. The results for two sub-wavelength modes of $\lambda/r \geq 70$ (namely highly suitable for near-field coupling and really in the quasi-static limit) at this optimal frequency are presented in Fig. 3. The two methods are again in very good agreement and show that expected quality factors in the microwave are $Q^{abs} \geq 1000$ and $Q^{rad} \geq 10,000$.

For the rate of energy transfer between two loops 1 and 2 at distance D between their centers (Fig. 4): numerically, the FEFD mode-solver simulations give κ again through the frequency splitting ($=2\kappa$) of the normal modes of the combined system; analytically, κ is

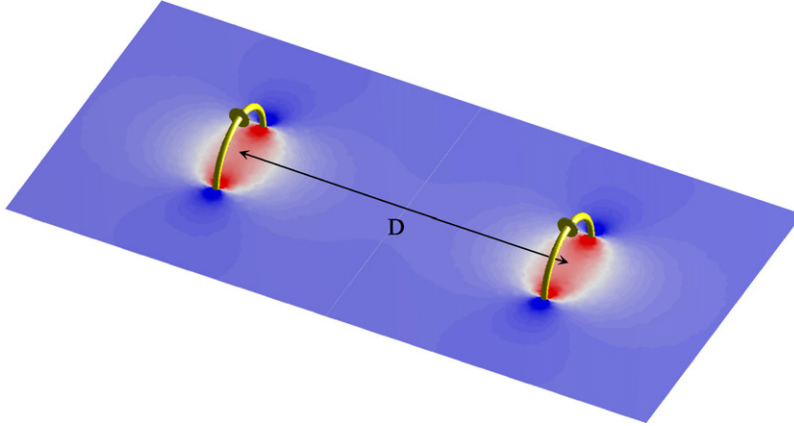


single loop	λ / r	Q^{rad}	Q^{abs}	$Q = \omega/2\Gamma$
r=30cm, a=2cm $\epsilon=10, A=138\text{cm}^2, d=4\text{mm}$	111.4 (112.4)	29546 (30512)	4886 (5117)	4193 (4381)
r=10cm, a=2mm $\epsilon=10, A=3.14\text{cm}^2, d=1\text{mm}$	69.7 (70.4)	10702 (10727)	1545 (1604)	1350 (1395)

Fig. 3. *Plot.* A wire loop of radius r connected to a pair of d -spaced parallel plates (shown in yellow) surrounded by air, along with a slice of the magnetic field (component parallel to the axis of the circular loop) of their resonant mode superimposed (shown in red/white/blue in regions of positive/zero/negative field respectively). *Table.* Numerical FEFD (and in parentheses analytical) results for the wavelength and absorption, radiation and total loss rates, for two different cases of subwavelength-loop resonant modes. Note that for conducting material copper ($\sigma = 5.998 \times 10^7$ S/m) was used. (*The specific parameters of the plot are highlighted with bold in the table.*) (For interpretation of the references to color in this figure legend, the reader is referred to the web version of this paper.)

given by $\kappa = \omega M / 2\sqrt{L_1 L_2}$, where M is the mutual inductance of the two loops, which, in the quasi-static limit $r \ll D \ll \lambda$ and for the relative orientation shown in Fig. 4, is $M \approx \pi / 2\mu_0 (r_1 r_2)^2 / D^3$ [14], which means that $\omega / 2\kappa \sim (D / \sqrt{r_1 r_2})^3$. Then, and for medium distances $D/r = 10-3$, the two methods agree well, and we finally find (Fig. 4) coupling-to-loss ratios, which peak at a frequency between those where the single-loop $Q_{1,2}$ peak and are in the range $\kappa/\Gamma \sim 0.5-50$.

It is important to appreciate the difference between such a resonant-coupling inductive scheme and the well-known non-resonant inductive scheme for energy transfer. Using CMT it is easy to show that, keeping the geometry and the energy stored at the source fixed, the resonant inductive mechanism allows for $\sim Q^2$ ($\sim 10^6$) times more power delivered for work at the device than the traditional non-resonant mechanism. This is why only close-range contact-less medium-power ($\sim W$) transfer is possible with the latter [2,3], while with resonance either close-range but large-power ($\sim kW$) transfer is allowed [4,5] or, as currently proposed, if one also ensures operation in the strongly-coupled regime, medium-range and medium-power transfer is possible. Capacitively-loaded conductive loops are actually being widely used also as resonant antennas (for example in cell phones), but those operate in the far-field regime with $D/r \gg 1, r/\lambda \sim 1$, and the radiation Q 's are intentionally designed to be small to make the antenna efficient, so they are not appropriate for energy transfer.



two loops	D/r	Q^{rad}	$Q = \omega/2\Gamma$	$\omega/2\kappa$	κ/Γ
$r=30\text{cm}$, $a=2\text{cm}$ $\epsilon=10$, $A=138\text{cm}^2$, $d=4\text{mm}$ $\lambda/r \approx 112$ $Q^{abs} \approx 4886$	3	30729	4216	62.6 (63.7)	67.4 (68.7)
	5	29577	4194	235 (248)	17.8 (17.6)
	7	29128	4185	589 (646)	7.1 (6.8)
	10	28833	4177	1539 (1828)	2.7 (2.4)
$r=10\text{cm}$, $a=2\text{mm}$ $\epsilon=10$, $A=3.14\text{cm}^2$, $d=1\text{mm}$ $\lambda/r \approx 70$ $Q^{abs} \approx 1546$	3	10955	1355	85.4 (91.3)	15.9 (15.3)
	5	10740	1351	313 (356)	4.32 (3.92)
	7	10759	1351	754 (925)	1.79 (1.51)
	10	10756	1351	1895 (2617)	0.71 (0.53)

Fig. 4. *Plot.* System of two same wire loops connected to parallel plates (yellow) for medium-distance D coupling between them, along with a slice of the magnetic field of the even normal mode superimposed (red/white/blue). Note that there is also an odd normal mode (not shown). *Table.* Numerical FEFD (and in parentheses analytical) results for the average wavelength and loss rates of the two normal modes (individual values not shown), and also the coupling rate and “strong/weak-coupling” figure-of-merit as a function of the coupling distance D , for the two cases of modes presented in Fig. 3. Note that the average Γ^{rad} shown are again slightly different from the single-loop value of Fig. 3, due to far-field interference effects present for the two normal modes, which again the analytical model cannot predict and thus analytical results for Γ^{rad} are not shown but the single-loop value is used. (The specific parameters of the plot are highlighted with bold in the table.) (For interpretation of the references to color in this figure legend, the reader is referred to the web version of this paper.)

3. Influence of extraneous objects

Clearly, the success of the proposed resonance-based wireless energy-transfer scheme depends strongly on the robustness of the objects’ resonances. Therefore, their sensitivity to the near presence of random non-resonant extraneous objects is another aspect of the proposed scheme that requires analysis. The appropriate analytical model now is that of perturbation theory (PT) [8], which suggests that in the presence of an extraneous object e the field amplitude $a_1(t)$ inside the resonant object 1 satisfies, to first order:

$$\frac{da_1}{dt} = -i(\omega_1 - i\Gamma_1)a_1 + i(\kappa_{1-e} + i\Gamma_{1-e})a_1 \tag{2}$$

where again ω_1 is the frequency and Γ_1 the intrinsic (absorption, radiation, etc.) loss rate, while κ_{11-e} is the frequency shift induced onto 1 due to the presence of e and Γ_{1-e} is the extrinsic due to e (absorption inside e , scattering from e , etc.) loss rate². The frequency shift is a problem that can be “fixed” rather easily by applying to every device a feedback mechanism that corrects its frequency (e.g. through small changes in geometry) and matches it to that of the source. However, the extrinsic loss can be detrimental to the functionality of the energy-transfer scheme, because it cannot be remedied, so the total loss rate $\Gamma_{1[e]} = \Gamma_1 + \Gamma_{1-e}$ and the corresponding figure-of-merit $\kappa_{[e]}/\sqrt{\Gamma_{1[e]}\Gamma_{2[e]}}$, where $\kappa_{[e]}$ the perturbed coupling rate, must be quantified.

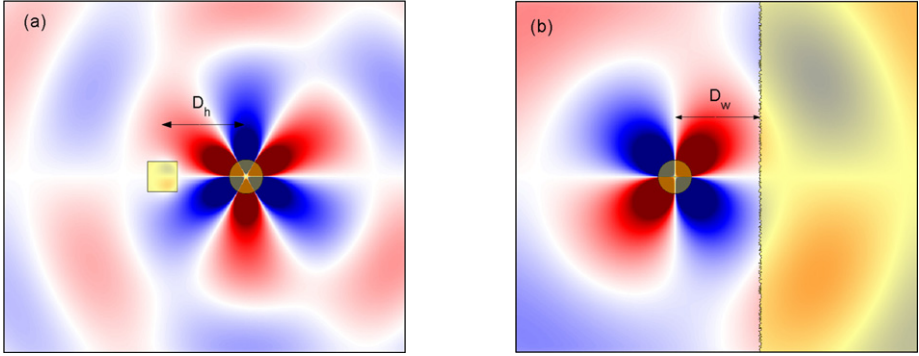
3.1. Dielectric disks

In the first example of resonant objects that we have considered, namely dielectric disks, small, low-index, low-material-loss or far-away stray objects will induce small scattering and absorption. In such cases of small perturbations these extrinsic loss mechanisms can be quantified using respectively the analytical first-order PT formulas $\Gamma_{1-e}^{\text{rad}} \propto \omega_1 \cdot \int d^3\mathbf{r} |\text{Re}\{\varepsilon_e(\mathbf{r})\}|^2 |\mathbf{E}_1(\mathbf{r})|^2 / U$ and $\Gamma_{1-e}^{\text{abs}} = \omega_1 / 4 \cdot \int d^3\mathbf{r} \text{Im}\{\varepsilon_e(\mathbf{r})\} |\mathbf{E}_1(\mathbf{r})|^2 / U$, where $U = 1/2 \cdot \int d^3\mathbf{r} \varepsilon(\mathbf{r}) |\mathbf{E}_1(\mathbf{r})|^2$ is the total resonant electromagnetic energy of the unperturbed mode. As one can see, both of these losses depend on the *square* of the resonant electric field tails \mathbf{E}_1 at the site of the extraneous object. In contrast, the coupling rate from object 1 to another resonant object 2 is, as stated earlier, $\kappa = \omega_1 / 4 \cdot \int d^3\mathbf{r} \varepsilon_2(\mathbf{r}) \mathbf{E}_2^*(\mathbf{r}) \mathbf{E}_1(\mathbf{r}) / U$ and depends *linearly* on the field tails \mathbf{E}_1 of 1 inside 2. This difference in scaling gives us confidence that, for exponentially small field tails, coupling to other resonant objects should be much faster than all extrinsic loss rates ($\kappa \gg \Gamma_{1-e}$), at least for small perturbations, and thus the energy-transfer scheme is expected to be sturdy for this class of resonant dielectric disks.

However, we also want to examine certain possible situations where extraneous objects cause perturbations too strong to analyze using the above first-order PT approach. For example, we place a dielectric disk c close to another off-resonance object of large $\text{Re}\{\varepsilon\}$, $\text{Im}\{\varepsilon\}$ and of same size but different shape (such as a human being h), as shown in Fig. 5a, and a roughened surface of large extent but of small $\text{Re}\{\varepsilon\}$, $\text{Im}\{\varepsilon\}$ (such as a wall w), as shown in Fig. 5b. For distances $D_{h/w}/r = 10-3$ between the disk-center and the “human”-center/“wall”, the numerical FDFD simulation results presented in Fig. 5 suggest that $Q_{c[h]}^{\text{rad}}, Q_{c[w]}^{\text{rad}} \geq 1000$ (instead of the initial $Q_c^{\text{rad}} \geq 2000$), $Q_c^{\text{abs}} \sim 10,000$ (naturally unchanged), $Q_{c-h}^{\text{abs}} \sim 10^5-10^2$, and $Q_{c-w}^{\text{abs}} \sim 10^5-10^4$, namely the disk resonance seems to be fairly robust, since it is not detrimentally disturbed by the presence of extraneous objects, with the exception of the *very* close proximity of high-loss objects [16].

To examine the influence of large perturbations on an entire energy-transfer system we consider two resonant disks in the close presence of both a “human” and a “wall”. The numerical FDFD simulations show that the system performance deteriorates from $\kappa/\Gamma_c \sim 1-50$ (Fig. 2) to $\kappa_{[hw]}/\Gamma_{c[hw]} \sim 0.5-10$ (Fig. 6), i.e. only by acceptably small amounts.

² The first-order PT model is valid only for small perturbations. Nevertheless, the parameters κ_{11-e} , Γ_{1-e} are well defined, even outside that regime, if a_1 is taken to be the amplitude of the exact perturbed mode.



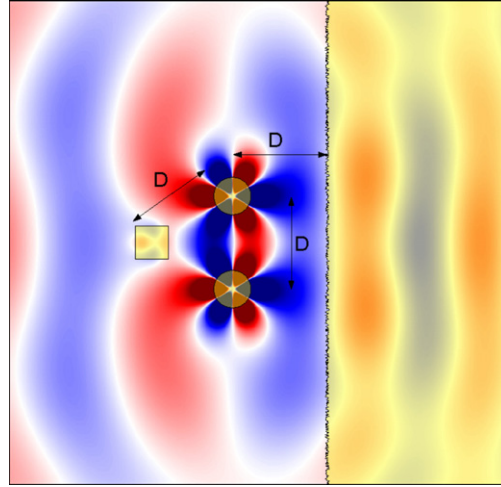
disk with “human”	D_h / r	Q_{c-h}^{abs}	$Q_{c[h]}^{rad}$	$Q_{c[h]}$
$Re\{\epsilon\}=147.7, m=2$ $\lambda / r \approx 20$ $Q_c^{abs} \approx 10096$	3	230	981	183
	5	2917	1984	1057
	7	11573	2230	1578
	10	41496	2201	1732
$Re\{\epsilon\}=65.6, m=3$ $\lambda / r \approx 10$ $Q_c^{abs} \approx 10096$	3	1827	6197	1238
	5	58431	11808	4978
	7	249748	9931	4908
	10	867552	9078	4754

disk with “wall”	D_w / r	Q_{c-w}^{abs}	$Q_{c[w]}^{rad}$	$Q_{c[w]}$
$Re\{\epsilon\}=147.7, m=2$ $\lambda / r \approx 20$ $Q_c^{abs} \approx 10098$	3	16725	1235	1033
	5	31659	1922	1536
	7	49440	2389	1859
	10	82839	2140	1729
$Re\{\epsilon\}=65.6, m=3$ $\lambda / r \approx 10$ $Q_c^{abs} \approx 10097$	3	53154	6228	3592
	5	127402	10988	5053
	7	159192	10168	4910
	10	191506	9510	4775

Fig. 5. Plots. A disk (yellow) in the proximity at distance $D_{h/w}$ of an extraneous object (yellow): (a) a high $\epsilon = 49 + 16i$ (which is large but actually appropriate for human muscles in the GHz regime [16]) square object of same size (area) with the disk, and (b) a large roughened surface of $\epsilon = 2.5 + 0.05i$ (appropriate for ordinary materials such as concrete, glass, plastic, wood [16]), along with the electric field of the disk’s perturbed resonant mode superimposed (red/white/blue). Tables. Numerical FDFD results for the parameters of the disk’s perturbed resonance, including absorption rate inside the extraneous object and total (including scattering from the extraneous object) radiation-loss rate, for the two cases of disk modes presented in previous figures. Note that again disk-material loss-tangent $Im\{\epsilon\}/Re\{\epsilon\}=10^{-4}$ was used, and that $Q_{c[h/w]}^{rad}$ is again different (decreased or even increased) from the single-disk Q_c^{rad} of Fig. 1, due to (respectively constructive or destructive) interference effects this time between the radiated and strongly scattered far-fields. (The specific parameters of the plots are highlighted with bold in the tables.) (For interpretation of the references to color in this figure legend, the reader is referred to the web version of this paper.)

3.2. Capacitively-loaded conducting-wire loops

In the second example of resonant objects that we have considered, the conducting-wire loops, the influence of extraneous objects on the resonances is nearly absent. The reason is that, in the quasi-static regime of operation ($r \ll \lambda$) that we are considering, the near field in the air region surrounding the loop is predominantly magnetic (since the electric field is localized inside the capacitor), therefore extraneous non-metallic objects e that could interact with this field and act as a perturbation to the resonance are those having significant magnetic properties (magnetic permeability $Re\{\mu\} > 1$ or magnetic loss $Im\{\mu\} > 0$). Since almost all every-day materials are non-magnetic, they respond to magnetic fields in the same way as free space, and thus will not disturb the resonance of a conducting-wire loop. To get only a rough estimate of this disturbance, we use the PT formula, stated earlier,



two disks with “human” and “wall”	D/r	Q_{c-h}^{abs}	Q_{c-w}^{abs}	$Q_{c[hw]}^{rad}$	$Q_{[hw]} = \omega/2\Gamma_{c[hw]}$	$\omega/2\kappa_{[hw]}$	$\kappa_{[hw]}/\Gamma_{c[hw]}$
$\text{Re}\{\varepsilon\}=147.7, m=2$ $\lambda/r \approx 20$ $Q_c^{abs} \approx 10100$	3	3300	12774	536	426	48	8.8
	5	5719	26333	1600	1068	322	3.3
	7	13248	50161	3542	2097	973	2.2
	10	18447	68460	3624	2254	1768	1.3
$\text{Re}\{\varepsilon\}=65.6, m=3$ $\lambda/r \approx 10$ $Q_c^{abs} \approx 10100$	3	2088	36661	6764	1328	141	9.4
	5	72137	90289	11945	4815	2114	2.3
	7	237822	129094	12261	5194	8307	0.6

Fig. 6. Plot. System of two same disks (yellow) for medium-distance D coupling between them in the proximity at equal distance D of two extraneous objects (yellow): both a high $\varepsilon = 49 + 16i$ square object of same size (area) with the disks and a large roughened surface of $\varepsilon = 2.5 + 0.05i$, along with the electric field of the system's perturbed even normal mode superimposed (red/white/blue). Table. Numerical FDFD results for the average wavelength and loss rates of the system's perturbed two normal modes (individual values not shown), and also the perturbed coupling rate and “strong/weak-coupling” figure-of-merit as a function of the distance D , for the two cases of disk modes presented in previous Figures. Only distances for non-radiative ($D < 2r_c$) coupling are considered. Note once more that the average Γ^{rad} takes into account interference effects between all radiated and scattered far-fields. (The specific parameters of the plot are highlighted with bold in the table.) (For interpretation of the references to color in this figure legend, the reader is referred to the web version of this paper.)

$\Gamma_{1-e}^{abs} = \omega_1/4 \cdot \int d^3\mathbf{r} \text{Im}\{\varepsilon_e(\mathbf{r})\} |\mathbf{E}_1(\mathbf{r})|^2 / U$ with the numerical results for the field of an example like the one shown in the plot of Fig. 4 and with a rectangular object of dimensions $30 \text{ cm} \times 30 \text{ cm} \times 1.5 \text{ m}$ and permittivity $\varepsilon = 49 + 16i$ (human muscles) residing between the loops and almost standing on top of one capacitor ($\sim 3 \text{ cm}$ away from it) and find $Q_{c-h}^{abs} \sim 10^5$ and for $\sim 10 \text{ cm}$ away $Q_{c-h}^{abs} \sim 5 \times 10^5$. Thus, for ordinary distances ($\sim 1 \text{ m}$) and placements (not immediately on top of the capacitor) or for most ordinary extraneous objects e of much smaller loss-tangent, we conclude that it is indeed fair to say that $Q_{c-e}^{abs} \rightarrow \infty$ and that $\kappa_{[e]}/\Gamma_{[e]} \sim \kappa/\Gamma \sim 0.5-50$. The only perturbation that is expected to affect these resonances is a close proximity of large metallic structures.

An extremely important implication of this fact relates to safety considerations for human beings. Humans are also non-magnetic and can sustain strong magnetic fields without undergoing any risk. A typical example, where magnetic fields $B \sim 1$ T are safely used on humans, is the magnetic resonance imaging (MRI) technique for medical testing. In contrast, the magnetic near-field required by our scheme in order to provide a few Watts of power to devices is only $B \sim 10^{-4}$ T, which is actually comparable to the magnitude of the Earth’s magnetic field. Since, as explained above, a strong electric near-field is also not present and the radiation produced from this non-radiative scheme is minimal, it is reasonable to expect that our proposed energy-transfer method should be safe for living organisms.

In comparison of the two classes of resonant systems under examination, the strong immunity to extraneous objects and the absence of risks for humans probably makes the conducting-wire loops the preferred choice for many real-world applications; on the other hand, systems of disks (or spheres) of high (effective) refractive index have the advantage that they are also applicable to much smaller length-scales (for example in the optical regime dielectrics prevail, since conductive materials are highly lossy).

4. Efficiency of energy-transfer scheme

Consider again the combined system of a resonant source s and device d in the presence of a set of extraneous objects e , and let us now study the efficiency of this resonance-based energy-transfer scheme, when energy is being drained from the device at rate Γ_{work} for use into operational work. The coupled-mode-theory equation for the device field-amplitude is

$$\frac{da_d}{dt} = -i(\omega - i\Gamma_{d[e]})a_d + i\kappa_{[e]}a_s - \Gamma_{\text{work}}a_d, \tag{3}$$

where $\Gamma_{d[e]} = \Gamma_{d[e]}^{\text{rad}} + \Gamma_{d[e]}^{\text{abs}} = \Gamma_{d[e]}^{\text{rad}} + (\Gamma_d^{\text{abs}} + \Gamma_{d-e}^{\text{abs}})$ is the net perturbed-device loss rate, and similarly we define $\Gamma_{s[e]}$ for the perturbed-source. Different temporal schemes can be used to extract power from the device (e.g. steady-state continuous-wave drainage, instantaneous drainage at periodic times and so on) and their efficiencies exhibit different dependence on the combined system parameters. Here, we assume steady state, such that the field amplitude inside the source is maintained constant, namely $a_s(t) = A_s e^{-i\omega t}$, so then the field amplitude inside the device is $a_d(t) = A_d e^{-i\omega t}$ with $A_d/A_s \sim i\kappa_{[e]}/(\Gamma_{d[e]} + \Gamma_{\text{work}})$. The various time-averaged powers of interest are then: the useful extracted power is $P_{\text{work}} = 2\Gamma_{\text{work}}|A_d|^2$, the radiated (including scattered) power is $P_{\text{rad}} = 2\Gamma_{s[e]}^{\text{rad}}|A_s|^2 + 2\Gamma_{d[e]}^{\text{rad}}|A_d|^2$, the power absorbed at the source/device is $P_{s/d} = 2\Gamma_{s/d}^{\text{abs}}|A_{s/d}|^2$, and at the extraneous objects $P_e = 2\Gamma_{s-e}^{\text{abs}}|A_s|^2 + 2\Gamma_{d-e}^{\text{abs}}|A_d|^2$. From energy conservation, the total time-averaged power entering the system is $P_{\text{total}} = P_{\text{work}} + P_{\text{rad}} + P_s + P_d + P_e$. Note that the reactive powers, which are usually present in a system and circulate stored energy around it, cancel at resonance (which can be proven for example in electromagnetism from Poynting’s Theorem [14]) and do not influence the power-balance calculations. The working efficiency is then:

$$\eta_{\text{work}} \equiv \frac{P_{\text{work}}}{P_{\text{total}}} = \frac{1}{1 + \frac{\Gamma_{d[e]}}{\Gamma_{\text{work}}} \cdot \left[1 + \frac{1}{\text{fom}_{[e]}} \left(1 + \frac{\Gamma_{\text{work}}}{\Gamma_{d[e]}} \right)^2 \right]}, \tag{4}$$

where $\text{fom}_{[e]} = \kappa_{[e]} / \sqrt{\Gamma_{s[e]} \Gamma_{d[e]}}$ is the distance-dependent figure-of-merit of the perturbed resonant energy-exchange system. Depending on the targeted application, reasonable choices for the work-drainage rate are: $\Gamma_{\text{work}} / \Gamma_{d[e]} = 1$ to minimize the required energy stored in the source, $\Gamma_{\text{work}} / \Gamma_{d[e]} = \sqrt{1 + \text{fom}_{[e]}^2} > 1$ to maximize the efficiency for some particular value of $\text{fom}_{[e]}$ or $\Gamma_{\text{work}} / \Gamma_{d[e]} \gg 1$ to minimize the required energy stored in the device. For any of these choices, η_{work} is a function of the $\text{fom}_{[e]}$ parameter only. η_{work} is shown for its optimal choice in Fig. 7 with a solid black line, and is $\eta_{\text{work}} > 17\%$ for $\text{fom}_{[e]} > 1$, namely large enough for practical applications. The loss conversion ratios depend also on the other system parameters, and the most disturbing ones (radiation and absorption in stray objects) are plotted in Fig. 7 for the two example systems of dielectric disks and conducting loops with values for their parameters within the ranges determined earlier.

To get a numerical estimate for a system performance, take, for example, coupling distance $D/r = 5$, a “human” extraneous object at distance $D_h/r = 10$, and that $P_{\text{work}} = 10 \text{ W}$ must be delivered to the load. Then, for dielectric disks we have (based on Fig. 5) $Q_{s[h]}^{\text{rad}} = Q_{d[h]}^{\text{rad}} \sim 10^3$, $Q_s^{\text{abs}} = Q_d^{\text{abs}} \sim 10^4$, $Q_{s-h}^{\text{abs}} = Q_{d-h}^{\text{abs}} \sim 5 \times 10^4$ and (based on Figs. 2 and 6) $\text{fom}_{[h]} \sim 3$, so from Fig. 7 we find efficiency $\eta_{\text{work}} = 52\%$ and that $P_{\text{rad}} \approx 8.3 \text{ W}$ will

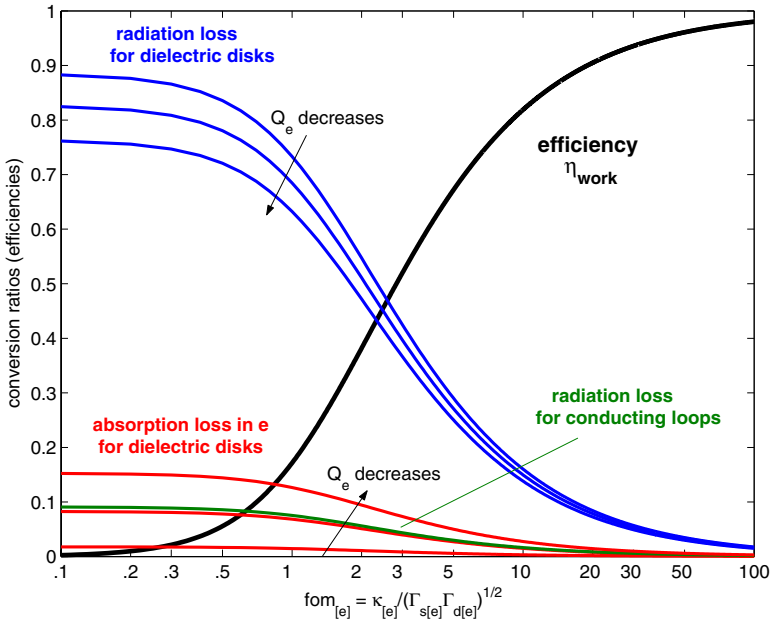


Fig. 7. *Black line.* Efficiency of converting the supplied power into useful work (η_{work}) as a function of the perturbed coupling-to-loss figure-of-merit, optimized with respect to the power-extracting rate Γ_{work} (related to the load impedance), for all values of the various quality factors that are present in the system. *Blue and red lines.* Ratios of power conversion respectively into radiation (including scattering from nearby extraneous objects) and dissipation inside an extraneous object as a function of the figure-of-merit for dielectric disks of $Q_{s[e]}^{\text{rad}} = Q_{d[e]}^{\text{rad}} \sim 10^3$ and $Q_s^{\text{abs}} = Q_d^{\text{abs}} \sim 10^4$, and for three values of $Q_{s-e}^{\text{abs}} = Q_{d-e}^{\text{abs}} = 10^4, 5 \times 10^4, 10^5$. *Green line.* Ratio of power conversion into radiation for conducting-wire loops of $Q_{s[e]}^{\text{rad}} = Q_{d[e]}^{\text{rad}} \sim 10^4$ and $Q_s^{\text{abs}} = Q_d^{\text{abs}} \sim 10^3$, and assuming $Q_{s-e}^{\text{abs}} = Q_{d-e}^{\text{abs}} \rightarrow \infty$. (For interpretation of the references to color in this figure legend, the reader is referred to the web version of this paper.)

be radiated to free space, $P_s \approx 0.5$ W will be dissipated inside the source, $P_d \approx 0.3$ W inside the device, and $P_h \approx 0.2$ W inside the human. On the other hand, for conducting loops we have (based on Figs. 3 and 4) $Q_{s[h]}^{\text{rad}} = Q_{d[h]}^{\text{rad}} \sim 10^4$, $Q_s^{\text{abs}} = Q_d^{\text{abs}} \sim 10^3$, $Q_{s-h}^{\text{abs}} = Q_{d-h}^{\text{abs}} \rightarrow \infty$ and $f_{[h]} \sim 4$, so we find $\eta_{\text{work}} = 61\%$, $P_{\text{rad}} \approx 0.6$ W, $P_s \approx 3.6$ W, $P_d \approx 2.2$ W, and most importantly $P_h \rightarrow 0$.

5. Conclusion

In conclusion, we present a scheme based on “strongly-coupled” resonances for mid-range wireless non-radiative energy transfer. Although our consideration has been for a static geometry (namely κ and Γ_e were independent of time), all the results can be applied directly for the dynamic geometries of mobile objects, since the energy-transfer time κ^{-1} (~ 1 – 100 μs for microwave applications) is much shorter than any timescale associated with motions of macroscopic objects. Analyses of very simple implementation geometries provide encouraging performance characteristics and further improvement is expected with serious design optimization. Thus the proposed mechanism is promising for many modern applications. For example, in the macroscopic world, this scheme could potentially be used to deliver power to robots and/or computers in a factory room, or electric buses on a highway (source-cavity would in this case be a “pipe” running above the highway). In the microscopic world, where much smaller wavelengths would be used and smaller powers are needed, one could use it to implement optical inter-connects for CMOS electronics, or to transfer energy to autonomous nano-objects (e.g. MEMS or nano-robots) without worrying much about the relative alignment between the sources and the devices.

As a venue of future scientific research, enhanced performance should be pursued for electromagnetic systems either by exploring different materials, such as plasmonic or metallo-dielectric structures of large effective refractive index, or by fine-tuning the system design, for example by exploiting the earlier mentioned interference effects between the radiation fields of the coupled objects. Furthermore, the range of applicability could be extended to acoustic systems, where the source and device are connected via a common condensed-matter object.

Acknowledgments

We thank Prof. John Pendry and L.J. Radziemski for suggesting magnetic and acoustic resonances respectively, and Prof. Steven G. Johnson, Prof. Peter Fisher, André Kurs and Miloš Popović for useful discussions. This work was supported in part by the Materials Research Science and Engineering Center program of the National Science Foundation under Grant No. DMR 02-13282, by the US Department of Energy under Grant No. DE-FG02-99ER45778, and by the Army Research Office through the Institute for Soldier Nanotechnologies under Contract No. DAAD-19-02-D0002.

References

- [1] N. Tesla, Apparatus for transmitting electrical energy, US patent number 1,119,732, issued in December 1914.
- [2] J.M. Fernandez, and J.A. Borras, Contactless battery charger with wireless control link, US patent number 6,184,651, issued in February 2001.

- [3] L. Ka-Lai, J.W. Hay, and P.G.W. Beart, Contact-less power transfer, US patent number 7,042,196, issued in May 2006 (SplashPower Ltd., <www.splashpower.com>).
- [4] A. Esser, H.-C. Skudelny, *IEEE Trans. Industry Appl.* 27 (1991) 872.
- [5] J. Hirai, T.-W. Kim, A. Kawamura, *IEEE Trans. Power Electron.* 15 (2000) 21.
- [6] G. Scheible, B. Smailus, M. Klaus, K. Garrels, and L. Heinemann, “System for wirelessly supplying a large number of actuators of a machine with electrical power”. *US patent* number 6,597,076, issued in July 2003 (ABB, <www.abb.com>).
- [7] A. Takao et al., *Nature* 443 (2006) 671.
- [8] H.A. Haus, *Waves and Fields in Optoelectronics*, Prentice-Hall, New Jersey, 1984.
- [9] D.M. Pozar, *Microwave Engineering*, Wiley, New Jersey, 2005.
- [10] M.V. Jacob, *Proc. IEEE TENCON 2003* 4 (2003) 1362.
- [11] H. Raether, *Surface Plasmons*, Springer-Verlag, Berlin, 1988.
- [12] D.F. Stevenpiper et al., *Phys. Rev. Lett.* 80 (1998) 2829.
- [13] COMSOL Inc. (<www.comsol.com>).
- [14] J.D. Jackson, *Classical Electrodynamics*, Wiley, New York, 1999.
- [15] C.A. Balanis, *Antenna Theory: Analysis and Design*, Wiley, New Jersey, 2005.
- [16] K. Fenske, D.K. Misra, *Appl. Microw. Wireless* 12 (2000) 92.